JOURNAL OF GEOPHYSICAL RESEARCH, VOL. 115, D01105, doi:10.1029/2009JD012490, 2010

Comparison of the tropical radiative flux and cloud radiative effect profiles in a climate model with Clouds and the Earth's Radiant Energy System (CERES) data

Wenying Su,[1,2] Alejandro Bodas-Salcedo,[3] Kuan-Man Xu,[2] and Thomas P. Charlock[2]

Received 15 May 2009; revised 4 August 2009; accepted 16 September 2009; published 7 January 2010.

[1] An insightful link of model performance to the physical assumptions in general circulation models (GCMs) can be explored if assessment of radiative fluxes and cloud radiative effects go beyond those at the top of the atmosphere (TOA). In this study, we compare the radiative flux profiles (at surface, 500 hPa, 200 hPa, 70 hPa, and TOA) and cloud effect profiles (500 hPa, 200 hPa, and TOA) from HadGAM1, using Surface and Atmospheric Radiation Budget (SARB) data from Clouds and the Earth's Radiant Energy System (CERES) on the TRMM satellite over the tropics (30°S–30°N). Comparison at TOA reveals that HadGAM1 agrees well with CERES for mean cloud height but lacks in cloudiness. Comparing to its predecessor, HadAM3, HadGAM1 agrees better with observations in TOA LW cloud effects, net cloud effects, and the ratio of SW to LW cloud effects. Extending the comparison to multiple levels, we gain additional insight into the vertical differences in clouds: for clouds at heights below 500 hPa, HadGAM1 and CERES are in good agreement in terms of cloudiness, but HadGAM1 underestimates the average cloud height; for clouds between 500 and 200 hPa, HadGAM1 underestimates the cloudiness but overestimates the average cloud height; for clouds at heights above 200 hPa, HadGAM1 produces more clouds than in CERES. Stratifying the cloud effects by dynamic regimes, we find that HadGAM1 underestimates cloudiness and overestimates averaged cloud height in the convective regimes, but the opposite is true in the strong subsidence regimes.

Citation: Su, W., A. Bodas-Salcedo, K.-M. Xu, and T. P. Charlock (2010), Comparison of the tropical radiative flux and cloud radiative effect profiles in a climate model with Clouds and the Earth's Radiant Energy System (CERES) data, *J. Geophys. Res.*, *115*, D01105, doi:10.1029/2009JD012490.

1. Introduction

[2] General circulation models (GCMs) are the primary tools used for climate change projections. Improving the confidence in GCMs has been the subject of effort for decades. According to recent comparison studies, cloud feedbacks are still the primary source for intermodel differences in climate sensitivity, with low clouds making the largest contribution to these differences [*Bony and Dufresne*, 2005].

[3] Extensive evaluations of clouds in GCMs have been done using satellite measured radiation budget at the top of the atmosphere (TOA) [*Harrison et al.*, 1990; *Kiehl and Ramanathan*, 1990; *Bony et al.*, 1992; *Pope et al.*, 2000; *Webb et al.*, 2001; *Allan et al.*, 2002; *Lu et al.*, 2004; *Martin et al.*, 2006]. These evaluations have focused on comparing monthly mean and annual mean distributions of TOA radiative fluxes and cloud radiative effects with those derived from Earth Radiation Budget Experiment (ERBE) [*Barkstrom et al.*, 1989] and Clouds and the Earth's Radiant Energy System (CERES) [*Wielicki et al.*, 1996], where cloud radiative effects are defined as the difference between clear- and all-sky fluxes. Recently, evaluations have focused on dynamically based cloud 'regimes' according to midtropospheric vertical velocity [*Norris and Weaver*, 2001; *Bony et al.*, 2004; *Yuan et al.*, 2008], surface pressure regimes [*Tselioudis et al.*, 2000], and a combination of midtropospheric vertical velocity with sea surface temperature [*Williams et al.*, 2003; *Ringer and Allan*, 2004].

[4] However, validations of radiative fluxes at the surface and within the atmosphere are also needed to assess various aspects of climate simulations. Surface radiation budget is routinely measured by ground-based networks, but these networks have very limited spatial coverage and can be used to assess fluxes for only a few model grid boxes [*Wild et al.*, 1995, 2006; *Bodas-Salcedo et al.*, 2008]. Global surface and atmospheric radiation budget can only be derived through radiative transfer modeling based on TOA measurements [*Rossow and Schiffer*, 1991; *Pinker and Laszlo*, 1992; *Zhang et al.*, 1995, 2004; *Whitlock et al.*, 1995; *Charlock et al.*, 2006]. For example, surface fluxes from the International

[1] Science Systems and Applications Inc., Hampton, Virginia, USA.
[2] NASA Langley Research Center, Hampton, Virginia, USA.
[3] Met Office, Hadley Center, Exeter, UK.

0148-0227/10/2009JD012490$09.00

Satellite Cloud Climatology Project (ISCCP) [*Rossow and Schiffer*, 1991] have been used to evaluate those from HadGAM1 [*Bodas-Salcedo et al.*, 2008]. *Webb et al.* [2001] combined ISCCP with ERBE to evaluate the fluxes and cloudiness in three GCMs. By decomposing the cloud radiative effects into contributions from low-, mid-, and high-level clouds, they found that low-level clouds in GCMs tended to compensate for the underestimation of the SW cloud radiative effect caused by a lack of high- and mid-level clouds, but failed to compensate for the LW radiative effect. *Williams et al.* [2005] applied the cluster technique to ISCCP-like diagnostics from two versions of the Hadley Center GCM to identify cloud regimes and to assess climate change response over four geographical regions. *Williams and Tselioudis* [2007] extended the analysis globally to six GCMs and showed that evaluation and subsequent improvement in the simulation of the present-day regime properties have the potential to reduce the variance of the global cloud response and climate sensitivity among GCMs.

[5] Although the ERBE-like product from CERES, which is produced using the ERBE algorithm [*Suttles et al.*, 1988, 1989], is widely used for GCM evaluation, other products from CERES are less exploited. The Surface and Atmospheric Radiation Budget (SARB) product (see section 2.2) provides fluxes at TOA, within the atmosphere, and at the surface. These flux profiles from SARB can be used to evaluate GCMs and to provide insight into the integrated effects of cloud and aerosol processes, as well as the distribution of water vapor, on fluxes at different levels in the models. The primary objective of this study is to use the CERES SARB product to evaluate model simulation of radiative flux profiles and cloud radiative effects at multiple levels. Some significant differences in the vertical distribution of clouds between model and observation are identified in this study that have not been revealed in previous studies using the TOA radiation budget data alone. The GCM, HadGAM1, that we evaluate in this study, CERES SARB data and the correction of its diurnal sampling are described in section 2. Flux and cloud effect comparison results, and the relationship of cloud effects to dynamic regimes are presented in section 3. Conclusions are given in section 4.

2. Data and Diurnal Sampling Adjustment

2.1. HadGAM1

[6] The latest climate configuration of the Met Office Unified Model (MetUM), referred to as HadGAM1, was used to simulate the present-day climate. HadGAM1 uses a horizontal resolution of 1.25° latitude by 1.875° longitude, and has 38 vertical levels, the top level being at around 39 km. The model is forced with observed sea surface temperatures (SSTs) from the second Atmospheric Model Intercomparison Project (AMIP-II) [*Gates et al.*, 1999]. The simulation started on December 1978, and we used diagnostics for 1998, when the TRMM CERES data were available.

[7] The dynamical core is a two-time level semi-implicit, semi-Lagrangian formulation and is also nonhydrostatic [*Davies et al.*, 2005]. The radiation code is that of *Edwards and Slingo* [1996] used in the previous Hadley Centre climate model, HadCM3, with improvements detailed below. The LW band from 1200 to 1500 cm^{-1} has been split at 1330 cm^{-1} in order to better represent the overlap between CH_4 and N_2O; gaseous absorption is based on the updated High-Resolution Transmission (HITRAN) 2000 database [*Rothman*, 2003]; the water vapor continuum, based on version 2.4 of the Clough-Kneizys-Davies (CKD) formulation [*Clough et al.*, 1992], has been included in the SW region; ice crystal sizes are parameterized as function of the environmental temperature [*Kristjánsson et al.*, 2000; *Edwards et al.*, 2007]; the sea surface albedo is based on the functional form of *Barker and Li* [1995], modified in light of aircraft data, and the land surface albedo is described by *Essery et al.* [2003]. Sulfate, fossil fuel black carbon, biomass-burning and sea salt aerosols are interactively simulated, as detailed by *Martin et al.* [2006]. A climatology for stratospheric sulfuric acid aerosol is used. The direct radiative effect (scattering and absorption of radiation) of all aerosols is included. Parameterizations of both first and second indirect aerosol effects (impact on cloud droplet size and on precipitation efficiency, respectively) are also included, with sulfate, biomass-burning and sea salt aerosols being considered cloud condensation nuclei; black carbon aerosols are assumed to be hydrophobic and so do not have indirect effects in HadGAM1. The radiation code uses the maximum/random overlap assumption for clouds. A more detailed description of HadGAM1 is given by *Martin et al.* [2006]. Its performance in terms of global climatology, variability and regional climate, and surface radiation budget can be found in the work of *Martin et al.* [2006], *Ringer et al.* [2006], and *Bodas-Salcedo et al.* [2008].

2.2. Clouds and the Earth's Radiant Energy System Surface and Atmospheric Radiation Budget Data

[8] The CERES instrument measures radiances in three channels: a broadband SW channel (0.3–5 μm), a window channel (8–12 μm), and a total channel (0.3–100 μm). The CERES radiances are converted to reflected SW, emitted LW, and emitted window (WN) fluxes at the TOA [*Loeb et al.*, 2003a], where the LW flux is the difference between the total and SW fluxes. The cloud and aerosol properties over the large CERES footprints ($\sim$10 km $\times$ 10 km) on the TRMM satellite are retrieved from the radiances from the smaller Visible Infrared Scanner (VIRS) pixels (2 km $\times$ 2 km) [*Wielicki et al.*, 1996].

[9] The SARB product from CERES provides estimates of SW, LW, and WN flux profiles using a fast, plane-parallel correlated- k radiative transfer code [*Fu and Liou*, 1992, 1993; *Rose and Charlock*, 2002]. SW and LW fluxes at the TOA, 70 hPa, 200 hPa, 500 hPa, and the surface are used in this study. Details of the SARB algorithm are described by *Charlock et al.* [2006] and *Su et al.* [2005, 2007], we briefly review the inputs for SARB calculation below.

[10] The most critical inputs for the calculations are cloud microphysical, macrophysical, and optical properties (cloud amount, cloud optical depth, cloud particle size and phase, liquid/ice water path, and effective radiating temperature) retrieved from VIRS imager pixel data. The retrieval algorithm assumed plane-parallel and single-layered clouds, details of the algorithm can be found in the work of *Minnis et al.* [1995, 1998, 2007, 2008]. Up to two distinct cloud layers are allowed in the large CERES footprints, but they may not overlap. Cloud amount derived from this algorithm agrees well with surface climatology, but is $\sim$0.07 less than cloud amount from ISCCP and MODIS science team anal-

Table 1. Biases of the Surface and Atmospheric Radiation Budget–Tuned All-Sky Top-of-Atmosphere and Surface Downwelling and Upwelling SW and LW Fluxes for January to August 1998 and the 8 Month Mean[a]

	Jan	Feb	Mar	Apr	May	Jun	Jul	Aug	Mean
TOA $S_a^{\uparrow}$	0.9	−0.1	−1.0	−0.3	−1.3	−0.1	−1.0	−0.2	−0.5
TOA $L_a^{\uparrow}$	0.1	0.2	−0.8	−1.1	−0.6	−1.4	−1.1	−2.2	−0.9
Surface $S_a^{\downarrow}$	14.4	9.6	12.7	8.6	16.5	10.3	13.4	17.2	13.8
Surface $S_a^{\uparrow}$	−5.7	−5.2	−7.3	−10.0	−6.4	−5.7	−6.8	−3.3	−6.1
Surface $L_a^{\downarrow}$	−11.1	−1.9	−6.2	−4.6	0.4	−2.3	−1.8	−6.1	−3.7
Surface $L_a^{\uparrow}$	−0.1	−5.1	−1.0	−1.4	−1.6	−0.7	−0.9	−6.8	−2.4

[a]Biases are in watts per meter squared. Biases are the differences between SARB fluxes and observations. Observations are from CERES for top-of-atmosphere upwelling fluxes and from ground-based radiometers for surface upwelling and downwelling fluxes. TOA is top of atmosphere.

yses, primarily as a result of missing small subpixel and thin clouds ($\tau < 0.3$).

[11] Aerosol optical depth (AOD) inputs to the radiative transfer model are from VIRS retrievals [*Ignatov and Stowe*, 2000], if available, or alternatively from the Model for Atmospheric Transport and Chemistry (MATCH) aerosol assimilation [*Collins et al.*, 2001]. Other data sets used including daily global ozone profiles from Stratosphere Monitoring Ozone Blended Analysis (SMOBA) (http://www.cpc.ncep.noaa.gov/products/stratosphere/SMOBA/), temperature and humidity profiles from European Center for Medium Range Weather Forecasts (ECMWF) operational analyses [*Rabier et al.*, 1998], and surface elevation from the U. S. Geological Survey GTOPO30 digital elevation model.

[12] SARB calculated SW and LW fluxes at the TOA have been validated using TOA fluxes from CERES, and SARB calculated upwelling and downwelling SW and LW fluxes at the surface have been validated using radiometer observed fluxes at 40 surface sites worldwide [*Rutan and Charlock*, 2004]. The biases (defined as calculation minus observation) of all-sky SW and LW fluxes at the TOA and surface are listed in Table 1 for January to August 1998 and for the 8 month mean (last column). These biases are obtained from the CERES validation web page (http://www-cave.larc.nasa.gov/cave/pages/valplot.html). SARB calculated reflected SW fluxes at the TOA are smaller than those from CERES observations, with the maximum bias of -1.3 Wm^{-2} and the 8 month mean bias of -0.5 W m^{-2}. SARB calculated emitted LW fluxes at the TOA are generally smaller than those from CERES, with the maximum bias of -2.2 W m^{-2} and the mean bias of -0.9 W m^{-2}. Biases of the surface fluxes are larger than those of TOA. The surface downwelling SW fluxes from SARB are larger than those from observations by 8.6 to 17.2 W m^{-2}, whereas the surface upwelling SW fluxes from SARB are smaller than those from observations by 3.3 to 10.0 W m^{-2}. The surface downwelling LW fluxes from SARB are smaller than those from observations, except for May, and the mean bias is -3.7 W m^{-2}. The surface upwelling LW fluxes from SARB are also smaller than those from observations, with a mean bias of -2.4 W m^{-2}.

[13] Validation of the flux profile within the atmosphere, however, is more challenging because of the lack of measurements. The only data source available for comparison is the Atmospheric Radiation Measurement (ARM) program's Broadband Heating Rate Product (BBHRP), which is designed to validate the radiative heating rates from GCMs [*Mlawer et al.*, 2004]. Cloud property inputs to the BBHRP are from a suite of ground-based instruments (active and passive) at the ARM Southern Great Plain central facility. *Rutan et al.* [2006] compared the flux profiles from SARB and BBHRP using 1 year data at the central facility. They found that the biases for the upwelling and downwelling SW flux in the atmosphere (at 500, 200, and 70 hPa) are about 15 and 5 W m^{-2}, and the biases for the upwelling and downwelling LW flux in the atmosphere are less than 5 and 3 W m^{-2}. Note these are instantaneous biases, if using monthly mean flux profiles, the biases are expected to be smaller. The good agreement between BBHRP and SARB downwelling SW and LW fluxes lends credence to the cloud retrievals used in SARB calculation, since BBHRP relies on active sensors (radar, lidar, ceilometer) to provide cloud profiles.

[14] In this study, we used the monthly gridded ($1^\circ \times 1^\circ$) data from hourly SARB flux profiles (Edition 2C). Unlike the ERBE-like product, whose clear-sky fluxes are based only upon scenes that are cloud-free [*Wong et al.*, 2000], SARB product are based upon redundant calculations using inputs for all, clear, and pristine sky in a manner that is consistent with GCMs. This avoids the undersampling of the humid cloudy regions as in the ERBE-like product, which tend to underestimate (overestimate) the actual SW (LW) cloud effects, because of additional water vapor absorption [*Allan et al.*, 2002; *Allan and Ringer*, 2003]. SARB calculations are constrained by the CERES TOA fluxes, which are based upon the angular distribution models developed for CERES on TRMM [*Loeb et al.*, 2003a] and are more accurate than the ERBE-like TOA fluxes: monthly regional mean biases are reduced from -2.73 to 0.03 W m^{-2} for SW flux and from 4.4 to 0.9 W m^{-2} for LW flux [*Loeb et al.*, 2003b].

2.3. Diurnal Sampling Adjustment for TRMM Satellite

[15] The TRMM satellite is on a precessing orbit with a cycle of about 46 days [*Wielicki et al.*, 1996]. The satellite overpasses low latitudes about once per day but at a different local time every day, which provides uneven diurnal coverage for a given location. This diurnal coverage is different from the regular time step used in models, which is 3 hours for the radiation code in HadGAM1. Therefore, the diurnal coverage of the CERES fluxes needs to be evaluated before we can compare these fluxes to their counterparts from HadGAM1.

[16] Figure 1 shows a histogram of cosine of solar zenith angle ($\cos\theta$) of the TRMM satellite (P_{trmm}), for July 1998 for a given grid box. To investigate how representative the TRMM diurnal coverage is, we also calculate the frequency of $\cos\theta$ corresponding to the "true" diurnal coverage (P_{actu}), shown as solid line in Figure 1. Because of the regular time step used in HadGAM1 and the fact that it uses the average $\cos\theta$ over the time step period, the model sampling resembles

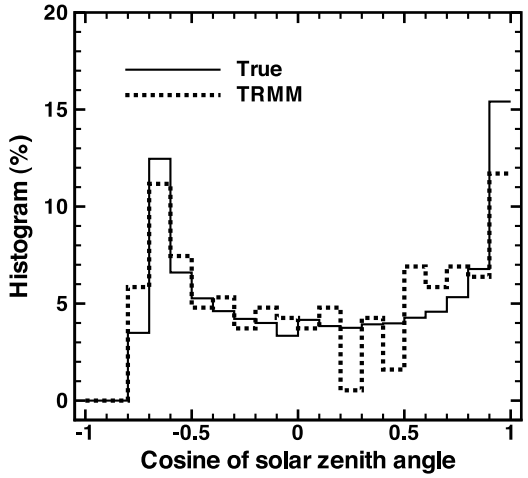

Figure 1. Histogram of cosine of solar zenith angle from TRMM satellite (dashed line) and calculated "true" diurnal coverage (solid line) at a given location for July 1998.

P_{actu} shown in Figure 1. P_{actu} and P_{trmm} agree reasonably well during nighttime, but differ significantly during daytime, indicating that the diurnal sampling of the TRMM satellite affects the SW and LW differently.

2.3.1. SW Adjustment Method

[17] To account for the insufficient daytime diurnal sampling of the TRMM satellite, we define the weight (α) for each cos θ bin:

$$\alpha(i) = \frac{P_{\text{actu}}(i)}{P_{\text{trmm}}(i)}, \tag{1}$$

where i is the bin number. All of the SW flux (S) measurements in a given month at a given location are first placed into cos θ bins, as shown in Figure 1. We then calculate the monthly mean SW flux by applying the weights to all SW flux measurements:

$$\overline{S} = \frac{1}{M_s}\sum_{j=1}^{M_s} S^j(i)\alpha(i), \tag{2}$$

where M_s is the total SW measurements in a month.

[18] The monthly mean TOA downwelling SW fluxes produced by this adjustment method agree with those from HadGAM1 to within ±2 W m^{-2}. We then multiply all SW fluxes by the ratio of TOA downwelling SW flux from HadGAM1 to that derived from SARB, thereby forcing the TOA downwelling SW fluxes to be identical between these two data sets. The estimated temporal sampling error after the adjustment is less than 10 W m^{-2} for monthly mean SW flux in a 1° × 1° region.

2.3.2. LW Adjustment Method

[19] *Lin et al.* [2002] studied the sampling rate of the TRMM satellite by incorporating its orbital information into the Colorado State University GCM. Their study showed that the sampling errors in monthly mean outgoing LW radiation (OLR) are typically within 4 W m^{-2} for each 2.25° × 2.25° grid box in the tropics (30°S to 30°N), and less than 0.4 W m^{-2} for the tropical monthly means. They suggested that errors over the subtropical continental grid boxes are due to uneven samplings of daytime and nighttime in the subtropics.

[20] We propose to adjust the weight of daytime and nighttime samples based upon the actual cos θ histogram and the TRMM cos θ histogram shown in Figure 1. Adjustment factors for daytime and nighttime are defined as:

$$\beta_{\text{day}} = \sum_{\cos\theta>0} \frac{P_{\text{actu}}}{P_{\text{trmm}}} \tag{3}$$

$$\beta_{\text{night}} = \sum_{\cos\theta\le 0} \frac{P_{\text{actu}}}{P_{\text{trmm}}}. \tag{4}$$

We then calculate the monthly mean LW flux by adjusting the weight of fluxes taking during daytime and nighttime:

$$\overline{L} = \frac{1}{M_l}\left(\sum_{j=1}^{M_s} L^j_{\text{day}}\beta_{\text{day}} + \sum_{j=1}^{M_l-M_s} L^j_{\text{night}}\beta_{\text{night}}\right), \tag{5}$$

where M_l is the total LW measurements in a month. The estimated uncertainty from the temporal sampling after the day-night adjustment is less than 4 W m^{-2} for monthly mean LW fluxes in a 1° × 1° region.

3. Results

3.1. Comparisons of the Monthly Tropical Mean Fluxes

[21] SW and LW fluxes from CERES and HadGAM1 have different spatial resolutions, and they are interpolated to 2° × 2° grids for comparison. We will use the following notation for radiative fluxes hereafter in this paper: S for monthly mean SW flux and L for monthly mean LW flux; the subscript denotes clear-sky (c) or all-sky (a); and the superscript denotes upwelling (↑) or downwelling (↓). We limited our analysis to the tropics (30°N to 30°S), because of the spatial coverage of the TRMM satellite.

3.1.1. SW Flux Comparison

[22] For clear-sky, the monthly tropical mean $S_c^{\downarrow}$ at the surface from CERES and HadGAM1 agree within 0.2 W m^{-2} for January and February. But the difference is 3 W m^{-2} in March and increases to 6 W m^{-2} for the summer months (CERES is smaller; not shown). Since clear-sky validations indicate that SARB overestimates surface $S_c^{\downarrow}$ (not included in Table 1), this suggests that aerosol loading in HadGAM1 is lower than that used in SARB calculation (either from VIRS retrieval or from MATCH), especially during the high dust season of the Sahara (June to August). Indeed, HadGAM1 does not have dust aerosols and its $S_c^{\downarrow}$ at the surface is more than 60 W m^{-2} higher than that from SARB in northern Africa (not shown).

[23] For all-sky, the monthly tropical mean $S_a^{\downarrow}$ at four selected levels are shown in Figure 2 for January to August 1998. Month to month changes in all fields are driven by the solar insolation at TOA, which is large in the tropics near the equinox. At 70 hPa, $S_a^{\downarrow}$ from HadGAM1 agree with SARB to within 0.5 W m^{-2}. At 200 hPa, $S_a^{\downarrow}$ from HadGAM1 are 0.6 to 1.5 W m^{-2} larger than those from SARB. At 500 hPa, however, the differences in $S_a^{\downarrow}$ increase to 7.6 to 12.7 W m^{-2}. These large differences are, as discussed later, likely caused

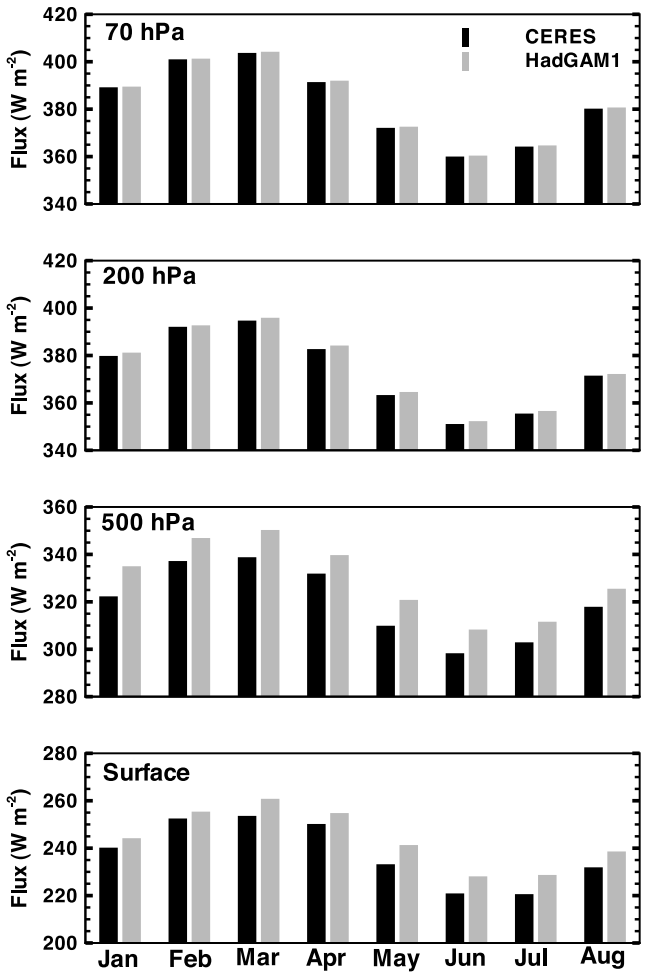

Figure 2. Tropical (30°N–30°S) monthly mean downwelling SW fluxes at 70 hPa, 200 hPa, 500 hPa, and the surface from Clouds and the Earth's Radiant Energy System (CERES) Surface and Atmospheric Radiation Budget (SARB) (black) and HadGAM1 (shaded) for all-sky conditions.

by the underprediction of cloudiness between 500 and 200 hPa in HadGAM1, compared to cloud properties used in the SARB calculation. At the surface, $S_a^{\downarrow}$ from HadGAM1 are 2.9 to 8.1 W m^{-2} larger than those from SARB. Since SARB overestimates surface $S_a^{\downarrow}$ (see Table 1), the actual biases of the surface $S_a^{\downarrow}$ in the model could be on the order of 10 to 20 W m^{-2}. *Bodas-Salcedo et al.* [2008] found that the HadGAM1 overestimates the surface $S_a^{\downarrow}$ by 5.8 to 48.5 W m^{-2} when compared with radiometer-measured fluxes in the tropics. The overestimation of surface insolation in HadGAM1 suggests there are fewer clouds and less aerosols (from clear -sky comparison) in the tropics compared to the retrievals used in SARB calculations.

[24] Despite the reasonable agreement for monthly tropical mean SW fluxes, there are large regional differences. Figure 3 shows the 3 month averaged $S_a^{\downarrow}$ differences (HadGAM1 minus SARB) at three levels (200 hPa, 500 hPa, and the surface) for JFM (January, February, and March) and JJA (June, July, and August), 1998. JFM represents the strong period of the 1997/98 El Niño, while JJA represents the subsequent dissipating period. In either period, the locations where large differences occur are in the major convective regions such as the intertropical convergence zone (ITCZ) and south Pacific convergence zone (SPCZ), and the stratocumulus regions (mainly at the surface). As in the tropical mean fluxes discussed earlier, the positive or negative differences at 500 hPa and the surface over ITCZ and SPCZ regions are significantly larger than those at 200 hPa, for example, between 60°E and 160°E in the Northern Hemisphere during JJA. Large positive differences over northern Africa, caused mainly by the lack of dust aerosols in HadGAM1, are noticeable at the surface during JJA. Detailed discussion and explanation of the regional differences will be given later in this section.

3.1.2. LW Flux Comparison

[25] Figure 4 shows the tropical monthly mean $L_a^{\uparrow}$ at five levels for January to August 1998. At the surface, $L_a^{\uparrow}$ from HadGAM1 are higher than those from SARB by 2 to 5 W m^{-2} for all 8 months. This indicates that the SSTs used in the HadGAM1 (which are from AMIP-II) [*Gates et al.*, 1999] are more realistic than those used in the SARB calculations, since SARB underestimates the surface $L_a^{\uparrow}$ (see Table 1). It is interesting to notice that $L_a^{\uparrow}$ from HadGAM1 and SARB agree within 2 W m^{-2} at 500 hPa. The differences gradually increase from 500 hPa to the TOA: $L_a^{\uparrow}$ from HadGAM1 are higher than those from SARB at the TOA by 5.6 to 9.0 W m^{-2}, which are much larger than the SARB $L_a^{\uparrow}$ uncertainties indicated in Table 1. The overestimation of $L_a^{\uparrow}$ by HadGAM1 is partly caused by its lack of cloudiness, and differences in temperature and humidity profiles between HadGAM1 and SARB (from ECMWF) may also contribute to the $L_a^{\uparrow}$ differences.

[26] Regional differences in $L_a^{\uparrow}$ are much larger than the tropical means (not shown). The surface $L_a^{\uparrow}$ differences are mainly over land and the differences over ocean are within 4 W m^{-2}. Spatial patterns of the $L_a^{\uparrow}$ differences at TOA are also associated with ITCZ and SPCZ, and similar to the patterns in the SW differences (Figure 3).

3.2. Comparisons of the Cloud Effects

[27] SW and LW cloud effects (often referred to as cloud radiative forcing) at a given level k are defined as

$$C_S^k = S_c^{k,\uparrow} - S_a^{k,\uparrow} \tag{6}$$

$$C_L^k = L_c^{k,\uparrow} - L_a^{k,\uparrow}. \tag{7}$$

The net cloud effect is

$$C_N^k = C_L^k + C_S^k. \tag{8}$$

To take advantage of the flux profiles, we investigate cloud effects between two levels: $\Delta C = C^{k+1} - C^k$. In this study, we focus on three layers (in addition to TOA): above 200 hPa ($\Delta C = C^{\mathrm{TOA}} - C^{200}$), between 200 and 500 hPa ($\Delta C = C^{200} - C^{500}$), and at 500 hPa ($C^{500}$). Also, the ratio of SW cloud effect to LW cloud effect, $N = -C_S/C_L$ (or $N = -\Delta C_S/\Delta C_L$), has been used to measure the relative magnitude of C_S and C_L (or ΔC_S and ΔC_L): if $N > 1$, then SW cooling dominates [*Cess et al.*, 2001a, 2001b]. Additionally, average of N over a large area serves as a measure of average cloud height ($\overline{H_c}$): smaller N for higher clouds.

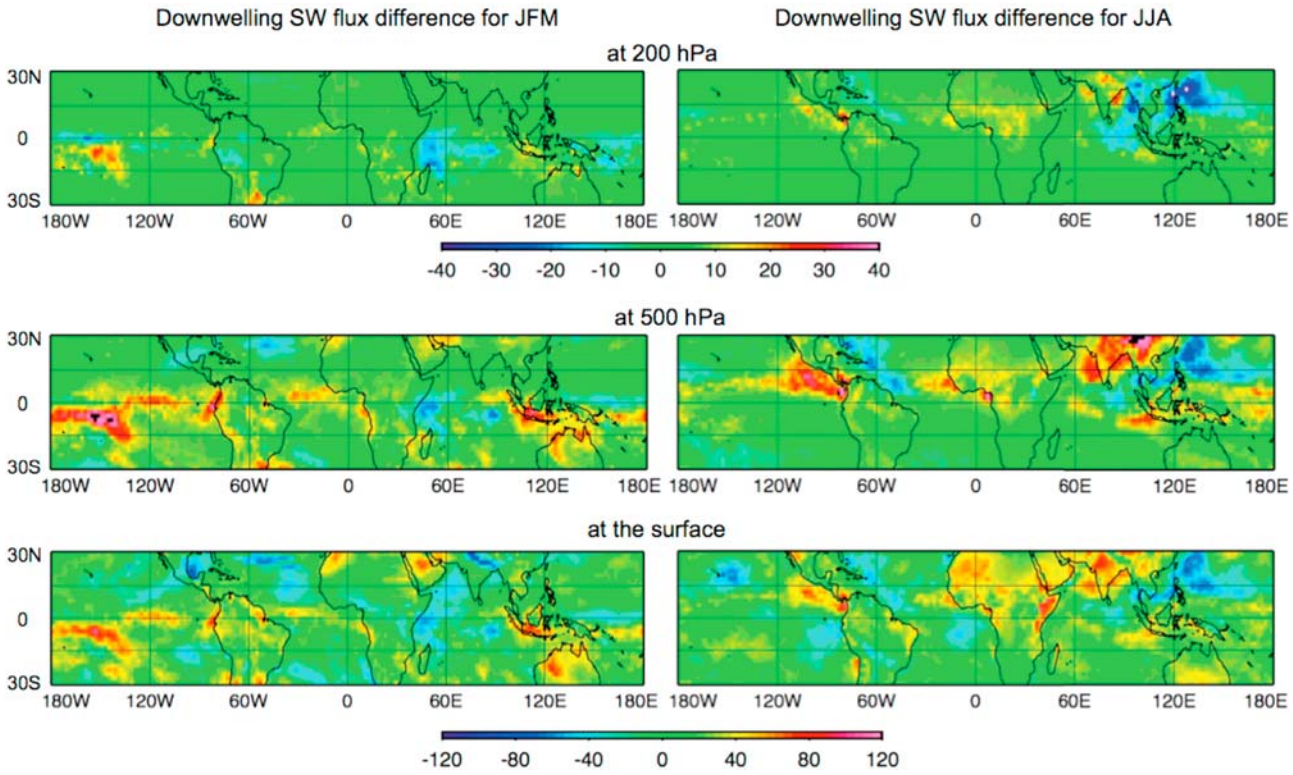

Figure 3. Three month mean downwelling SW flux differences (HadGAM1 minus CERES SARB) at 200 hPa, 500 hPa, and the surface for all-sky conditions. (left) Average differences for JFM (January, February, and March) and (right) average differences for JJA (June, July, and August). (top) Differences at 200 hPa (scales are shown in the color bar right below). (middle, bottom) Differences at 500 hPa and the surface (scales are shown in the color bar at the bottom), respectively. Units are watts per meter squared.

3.2.1. Tropical Mean Cloud Effects

[28] The tropical 8 month mean cloud radiative effects and the ratio N at TOA derived from CERES SARB product and from HadGAM1 are listed in Table 2; these parameters derived from CERES ERBE-like product and HadAM3 by *Allan et al.* [2002] are also included. It is apparent that the differences in cloud effects between SARB and ERBE-like products are caused by the undersampling of the humid cloudy regions by ERBE-like product, as discussed in section 2.2. The differences in C_L, C_N, and N between SARB and HadGAM1 are much smaller than those between SARB and HadAM3. This result suggests that HadGAM1 has a better skill than HadAM3 in simulations of cloud radiative effects at the TOA, because the cloud schemes used in HadGAM1 produces more realistic cloud coverages than HadAM3 [*Martin et al.*, 2006], and HadGAM1 simulates more clouds of intermediate optical depths than HadAM3 due to the inclusion of a parameterization for convective anvils [*Ringer and Allan*, 2004].

[29] To gain further insights into the improved simulations of cloud radiative effects, Figure 5 partitions the tropical monthly mean SW and LW cloud effects according to different layers in the atmosphere: the total lengths of the bars are the TOA cloud effects, the total lengths of the white bars are the cloud effects above 200 hPa, the total lengths of the gray bars are the cloud effects between 200 and 500 hPa, and the total lengths of the black bars are the cloud effects below 500 hPa. The tropical 8 month mean cloud effects and N values for these three layers are listed in Table 3. Also, relationships between monthly mean N and C_N are presented in Figure 6: blue symbols show the relationship at TOA, red symbols at 500 hPa, and green symbols between 500 and 200 hPa.

[30] As in the 8 month mean TOA cloud radiative effects, the monthly mean TOA cloud effects show a good agreement (Figure 5). The TOA C_L from HadGAM1 agree with those from SARB to within 1.2 W m^{-2}, except for January. The TOA $|C_S|$ from HadGAM1 are smaller than those from SARB, with the largest differences ($\sim$4 W m^{-2}) occurred during the strong El Niño months, and the smallest differences (<2 W m^{-2}) during the months of May to August, suggesting that CERES retrieves more and/or thicker clouds than produced in HadGAM1. This underestimation of cloudiness in HadGAM1 is also noted by *Martin et al.* [2006] and *Bodas-Salcedo et al.* [2008]. The N values agree to within 8% as seen in Figure 6 (blue symbols), indicating the agreement between the monthly averaged $\overline{H_c}$ from HadGAM1 and CERES is exceptionally good, although HadGAM1 underestimates the net cooling effects (see also the 8 month mean C_N in Table 2).

[31] Although evaluation of cloud effects is traditionally done at the TOA as in the preceding paragraph, we take a step further by comparing cloud effects at different levels to evaluate the vertical distributions of clouds in a few layers. At 500 hPa, the 8 month mean $|C_S|$, C_L and C_N between HadGAM1 and CERES agree to within 1 W m^{-2} (Table 3).

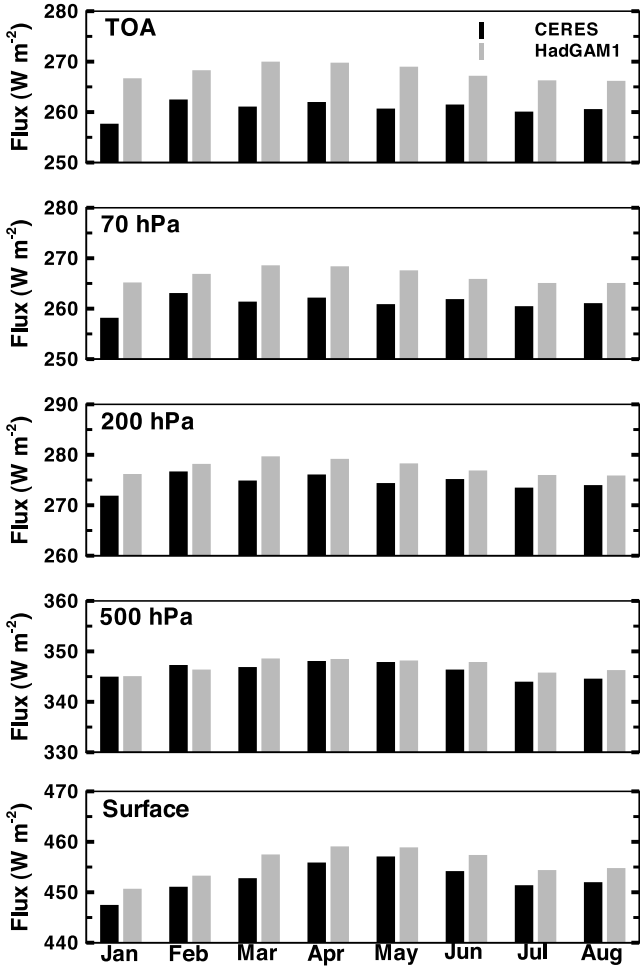

Figure 4. Tropical (30°N–30°S) monthly mean upwelling longwave fluxes at the surface, 500 hPa, 200 hPa, 70 hPa, and top of atmosphere (TOA) from CERES SARB (black) and HadGAM1 (gray) for all-sky conditions.

This agreement may indicate that either HadGAM1 has similar cloud amount and optical depth at height below 500 hPa as in CERES cloud retrieval, or some compensating effects between cloud amount and optical depth, or compensating regional cloud effects in the model. However, Figure 5 shows that monthly mean C_L from HadGAM1 are smaller at 500 hPa (though monthly mean $|C_S|$ from HadGAM1 are slightly larger). This suggests that clouds below 500 hPa in HadGAM1 are lower than the retrievals used in SARB, which is also confirmed in Figure 6 (red symbols). Furthermore, Figure 5 reveals greater differences between HadGAM1 and SARB in cloud radiative effects for layer between 500 and 200 hPa than at 500 hPa. For the layer between 500 and 200 hPa, monthly mean $|C_S|$ from HadGAM1 are smaller than those from SARB (up to 6 W m^{-2}), suggesting that HadGAM1 produces fewer and/or thinner clouds in this layer than the retrievals used in SARB calculations. The relationship between N and C_N for this layer (green symbols in Figure 6) shows that clouds between 500 and 200 hPa are consistently higher in HadGAM1, and there is modest net cooling in SARB but more cancellation between SW cooling and LW warming in HadGAM1 (see also the 8 month mean C_N in Table 3). The overestimated cloudiness above 200 hPa, as inferred from larger $|C_S|$ above 200 hPa in HadGAM1 than in SARB (Figure 5), do not compensate for the underestimation of cloudiness (and/or thinner clouds) between 500 and 200 hPa, resulting in an underestimation of $|C_S|$ at the TOA. The small C_L above 200 hPa from HadGAM1 are almost nonexistent in SARB. Though the layers used in our comparison are different from the cloud top pressures used in the clustering analysis by *Williams and Tselioudis* [2007], the results from our study are qualitatively consistent with their results, i.e., deep convective clouds and thin cirrus from HadGAM1 are higher and thicker, and mid-level convective clouds are totally missed in HadGAM1.

[32] A note of caution should be made regarding cloud height retrievals using passive satellite sensor. Comparing to active sensor, passive sensor tends to underestimate the cloud top height for clouds above 5 km and overestimate it for low-level marine stratus [*Holz et al.*, 2008]. The underestimation of thin cirrus cloud top height by passive sensor was also noted by comparing to ground-based cloud radar measurements [*Mace et al.*, 2005]. Other shortcomings in cloud retrieval algorithms could, to some extent, contribute to the cloud height and cloud effect differences between CERES and HadGAM1, except at the TOA where SARB all-sky fluxes are constrained by CERES observations.

[33] In summary, HadGAM1 agrees well with SARB for mean cloud height but produces less and/or thinner clouds than SARB in the tropics for all the months considered. Breaking these differences into three vertical layers, we find that: for clouds at heights below 500 hPa, SARB and HadGAM1 agree well in terms of cloud amount and optical depth (or compensating effects between them in HadGAM1) but clouds are lower in HadGAM1; between 500 and 200 hPa, HadGAM1 tends to have less and/or thinner, but higher clouds; and HadGAM1 has more clouds at heights above 200 hPa than in SARB.

3.2.2. Regional Cloud Effects

[34] Though monthly tropical mean cloud radiative effects from HadGAM1 agree well with those from SARB, large regional differences remain. Figures 7 and 8 show the TOA SW and LW cloud effects from SARB and HadGAM1 for March and July. In general, HadGAM1 reproduces the spatial distribution of C_S and C_L for both months reasonably well. In March, the maxima in $|C_S|$ from SARB are associated with the ITCZ and SPCZ while this association is less obvious in HadGAM1 (Figure 7, top); SARB and HadGAM1 agree on the location of a monsoon in equatorial South America. However, the contrast in C_L between SARB and HadGAM1

Table 2. January–August Tropical (30°N–30°S) Mean SW, LW, and Net Cloud Effects and the Ratio of SW to LW Cloud Effect (N) Derived From Clouds and the Earth's Radiant Energy System Surface and Atmospheric Radiation Budget Product and HadGAM1 at the TOA and Those Derived Using CERES ERBE-like Product and HadAM3 From *Allan et al.* [2002][a]

	C_S	C_L	C_N	N
SARB	−44.3	25.2	−19.1	1.76
HadGAM1	−42.0	24.6	−17.4	1.71
ERBE-like	−43.7	28.4	−15.3	1.54
HadAM3	−45.9	22.4	−23.5	2.05

[a]Cloud effects are in watts per meter squared. Abbreviations are as follows: ERBE, Earth Radiation Budget Experiment, and SARB, Surface and Atmospheric Radiation Budget.

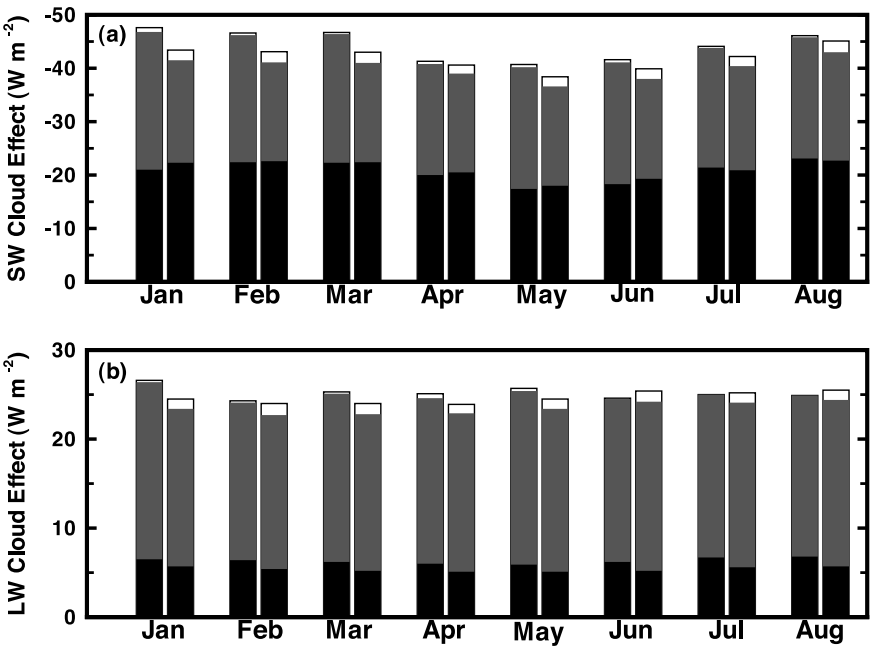

Figure 5. Tropical (30°N–30°S) monthly mean (a) SW cloud effect and (b) LW cloud effect. For each month, the bars on the left are for CERES SARB and the bars on the right are for HadGAM1. From 0 to the top of the white bars are the cloud effects at TOA, the total lengths of the white bars are the cloud effects above 200 hPa, the total lengths of the shaded bars are the cloud effects between 500 and 200 hPa, and the total lengths of the black bars are the cloud effects at 500 hPa.

(Figure 8, top) is smaller than that in $|C_S|$, suggesting that the agreement between SARB and HadGAM1 in cloud top height is better than the agreement in cloud amount and/or optical depth. The HadGAM1 captures the spatial distribution of $|C_S|$ minima reasonably well, but generally underestimates them. Though there are large difference in $|C_S|$ over the Arabian Sea, the C_L agrees well. This may indicate that the difference in $|C_S|$ is mostly from low clouds. In July, HadGAM1 captures the $|C_S|$ maxima occur over the Californian stratocumulus region, tropical east Pacific, central Africa, over India and the Southeast Asia, but underestimates these maxima. On the other hand, HadGAM1 overestimates the $|C_S|$ over the tropical warm pool region. SARB locates the monsoon near Central America, while HadGAM1 moves the action off the northeastern coast of Brazil. The Asian monsoon is more heavily maritime in HadGAM1 than in SARB.

[35] More insights on the model may be obtained by extending the comparison of cloud effects to layers within the atmosphere. Figures 9 and 10 show ΔC_S and ΔC_L between different levels derived from SARB and HadGAM1 for March 1998. The distribution of the cloud effects between TOA and 200 hPa is mainly associated with the ITCZ, and HadGAM1 has more and higher clouds above 200 hPa over the ITCZ, as noted earlier in the tropical mean results. The distribution of cloud effects between 200 and 500 hPa again reflects the ITCZ and SPCZ: SARB has more and higher clouds between these two levels over the Pacific portion of the ITCZ, but has fewer clouds off the east coast of South Africa. The distribution of cloud effects at 500 hPa bears no resemblance to that of the ITCZ, and the cloud effects from SARB and HadGAM1 agree well in general, as in the tropical mean results, except that there are more and higher clouds off the west coasts of Mexico and Chile from SARB data.

[36] In July, HadGAM1 has more and higher clouds over 200 hPa over the Bay of Bengal, southeast Asia, South China Sea, western Pacific, and to the east of the Caribbean islands, but has fewer over central Africa (not shown). We also note other aspects of the in-atmosphere cloud effects in July: in both SARB and HadGAM1, the distributions of cloud effects between 500 and 200 hPa are associated with the ITCZ, in addition to the strong cloud effects over the Bay of Bengal and Indian Ocean. SARB has more and higher clouds between these two levels over the west coast of central America, India, and southeast Asia; but HadGAM1 has more

Table 3. January–August Tropical (30°N–30°S) Mean SW, LW, and Net Cloud Effects From Clouds and the Earth's Radiant Energy System SARB Product and HadGAM1 for Three Layers: Above 200 hPa, Between 200 and 500 hPa, and at 500 hPa[a]

	ΔC_S	ΔC_L	ΔC_N	N
	Above 200 hPa			
SARB	−0.4	0.2	−0.2	2.00
HadGAM1	−1.9	1.1	−0.8	1.73
	Between 200 and 500 hPa			
SARB	−23.2	18.7	−4.5	1.24
HadGAM1	−19.0	18.1	−0.9	1.05
	At 500 hPa			
SARB	−20.7	6.3	−14.4	3.29
HadGAM1	−21.1	5.4	−15.7	3.91

[a]Cloud effects are in watts per meter squared. For each layer, N is defined as $-\Delta C_S/\Delta C_L$.

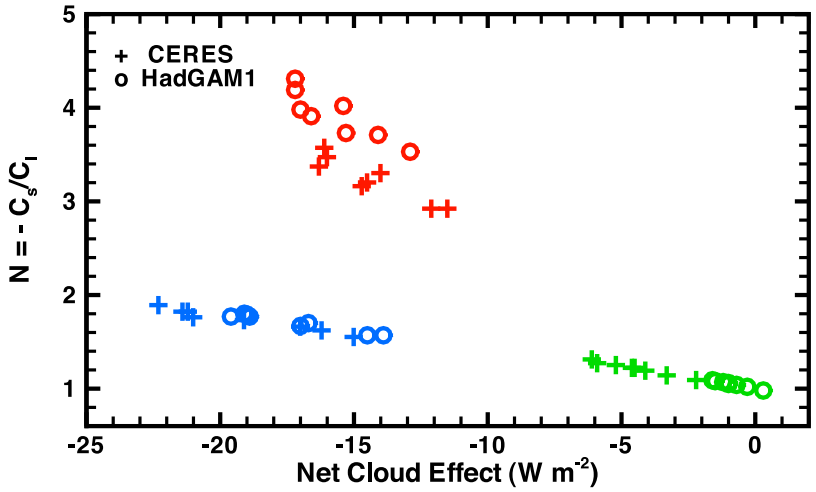

Figure 6. Tropical (30°N–30°S) monthly mean scatterplot of N versus net cloud effects derived from CERES (plusses) and from HadGAM1 (circles): red symbols are for N and the net cloud effect at 500 hPa, green symbols are for the same between 500 and 200 hPa, and blue symbols are for TOA.

and higher clouds over the Bay of Bengal and the South China Sea. Strong cloud effects at 500 hPa occur mostly along the coasts in both SARB and HadGAM1: HadGAM1 underestimates the stratocumulus cloud radiative effect off the Californian coast, though overestimates the cloud top height; and the opposite is true off the west coasts of Africa and south America.

3.3. Relationships of Cloud Effects to Dynamic Regimes

[37] To investigate the relationships of cloud effects to dynamic regimes, we follow the method of *Bony et al.* [2004] by stratifying the cloud effects according to the 500 hPa vertical velocity (ω_{500}, in unit hPa d^{-1}). Cloud effects from SARB are stratified by ω_{500} from the ECMWF ERA Interim reanalysis [*Uppala et al.*, 2008], while those of HadGAM1 are stratified by its own ω_{500}.

[38] The stratified TOA C_S, C_L, C_N, and N are shown in Figure 11 for the 8 month period. The median values of $|C_S|$ from HadGAM1 are 20 to 10 W m^{-2} smaller than those from SARB for the strong convective regimes, but are similar for the subsidence regimes. The median values of C_L from HadGAM1 are 5 to 12 W m^{-2} smaller than those from SARB for the strong convective regimes and only slightly smaller for the subsidence regimes. The median values of C_N from HadGAM1 are more or less constant across the circulation regimes, whereas those from SARB are strongly dependent upon the circulation regimes, with 10 to 15 W m^{-2} stronger cooling than in HadGAM1 for convective regimes with $\omega_{500} < -60$ hPa d^{-1}. Also, HadGAM1 underestimates the maximum cooling effects in the convective regimes but overestimates them in the subsidence regimes, whereas HadAM3 overestimated C_N across all dynamic regimes when compared with ERBE data [*Bony et al.*, 2004].

[39] Furthermore, box plot provides more details on the cloud differences between HadGAM1 and SARB. Judging from the 5th percentiles of $|C_S|$, SARB has more and/or thicker clouds than HadGAM1 in the convective regimes, but

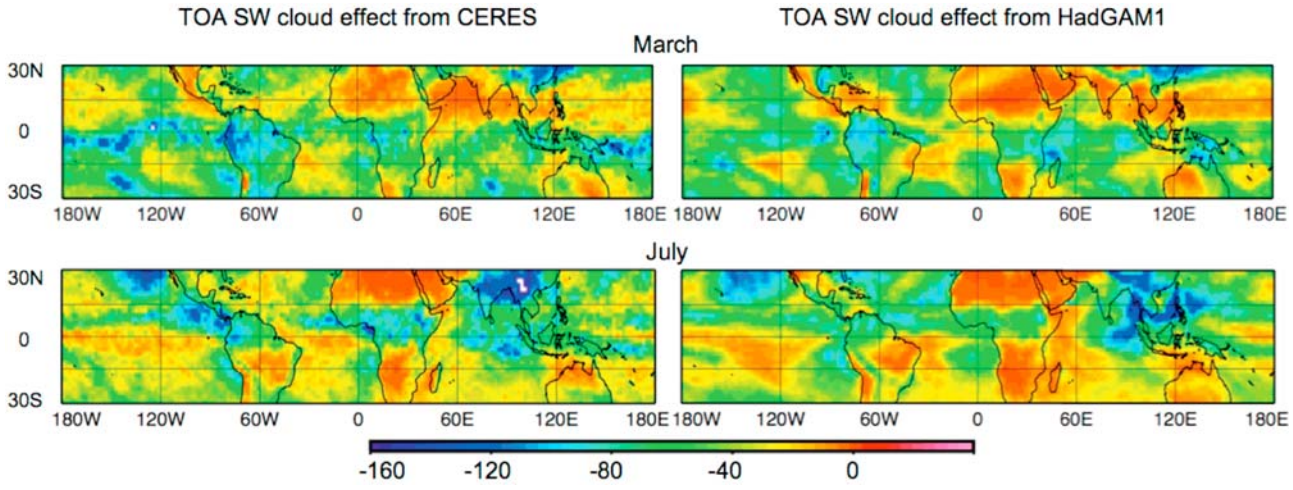

Figure 7. TOA SW cloud effect for (top) March and (bottom) July 1998. (left) CERES SARB and (right) HadGAM1. Units are watts per meters squared.

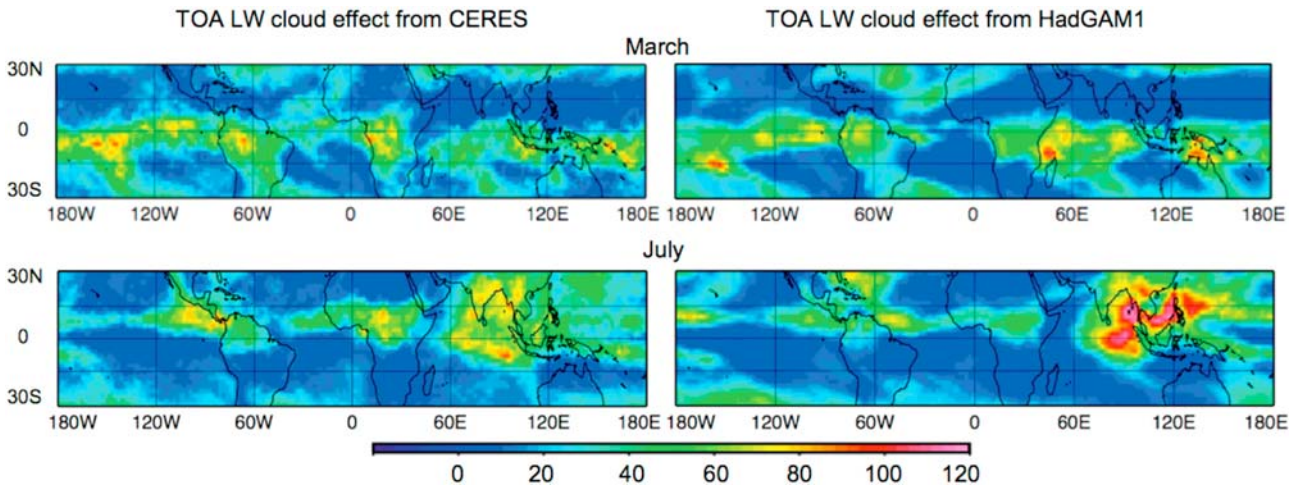

Figure 8. TOA LW cloud effect for (top) March and (bottom) July 1998. (left) CERES SARB and (right) HadGAM1. Units are watts per meters squared.

has less and/or thinner clouds in the subsidence regimes. The 95th percentiles of C_L from HadGAM1 are much higher than those from SARB, suggesting that HadGAM1 produces more high clouds than the retrievals used in SARB across all dynamic regimes. The ranges of C_N from HadGAM1 are smaller than those from SARB for convective regimes, indicating more cancellation between C_S and C_L in HadGAM1 than in SARB over the convective regimes. This is supported by the smaller median values and smaller ranges of N from HadGAM1 for the convective regimes. However, the N ranges from HadGAM1 are larger than those from SARB for the subsidence regimes. The larger N ranges between the first and third quartiles in HadGAM1 over the subsidence regimes suggest that its skill in simulating the boundary layer clouds is more limited, compared to its ability to simulate the deep convective clouds.

[40] The wide ranges of C_N and N associated with strong negative ω_{500} indicate that there are cloud types other than deep convective (which typically have $N > 1$ and $C_N < 0$), for example, thin cirrus ($N < 1$ and $C_N > 0$), although thin cirrus only accounts for ~5% of the cloud effects (judging from the 95th percentiles of C_N and the 5th percentiles of N in Figure 11). Another interesting feature in Figure 11 is that there are more occurrences of net warming at TOA by clouds in the subsidence regimes than in the convective regimes. SARB data indicate that the occurrence frequency of this phenomenon is ~7% and mainly over northern Africa, where the SW (LW) cloud effects are diminished (enhanced) by

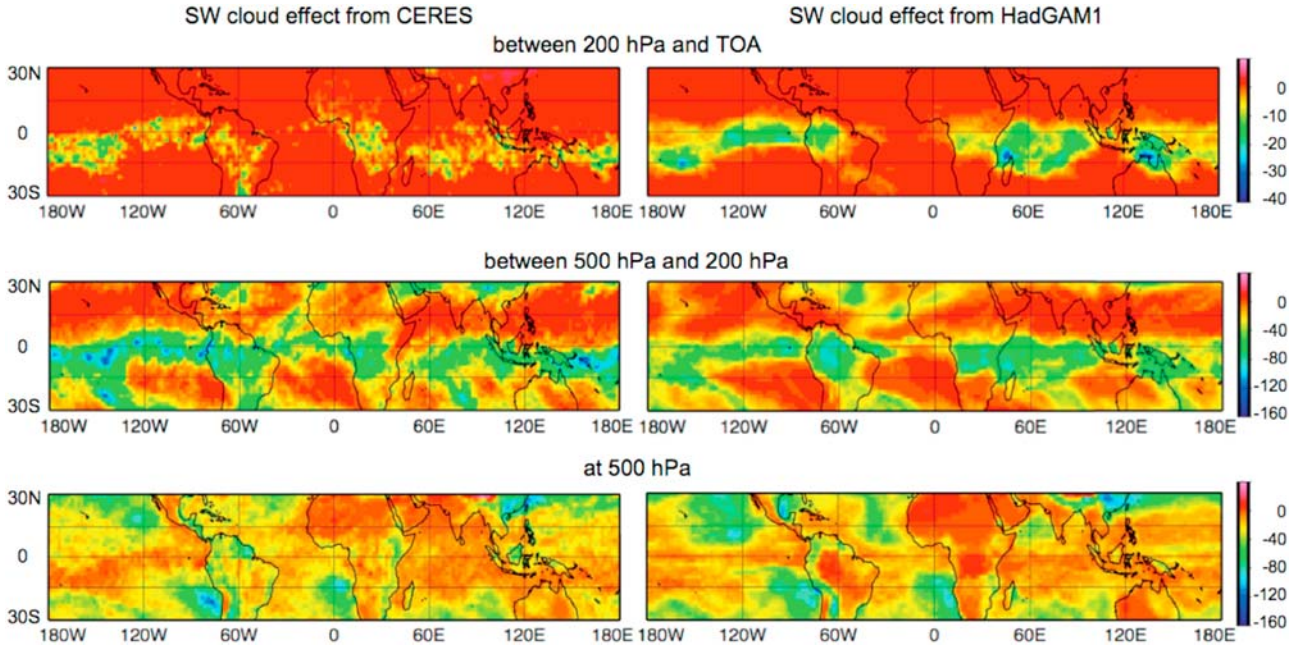

Figure 9. SW cloud effect between different levels for March 1998. (left) CERES SARB and (right) HadGAM1. (top) Cloud effects between 200 hPa and TOA; (middle) cloud effects between 500 hPa and 200 hPa; (bottom) cloud effects at 500 hPa. Units are watts per meters squared.

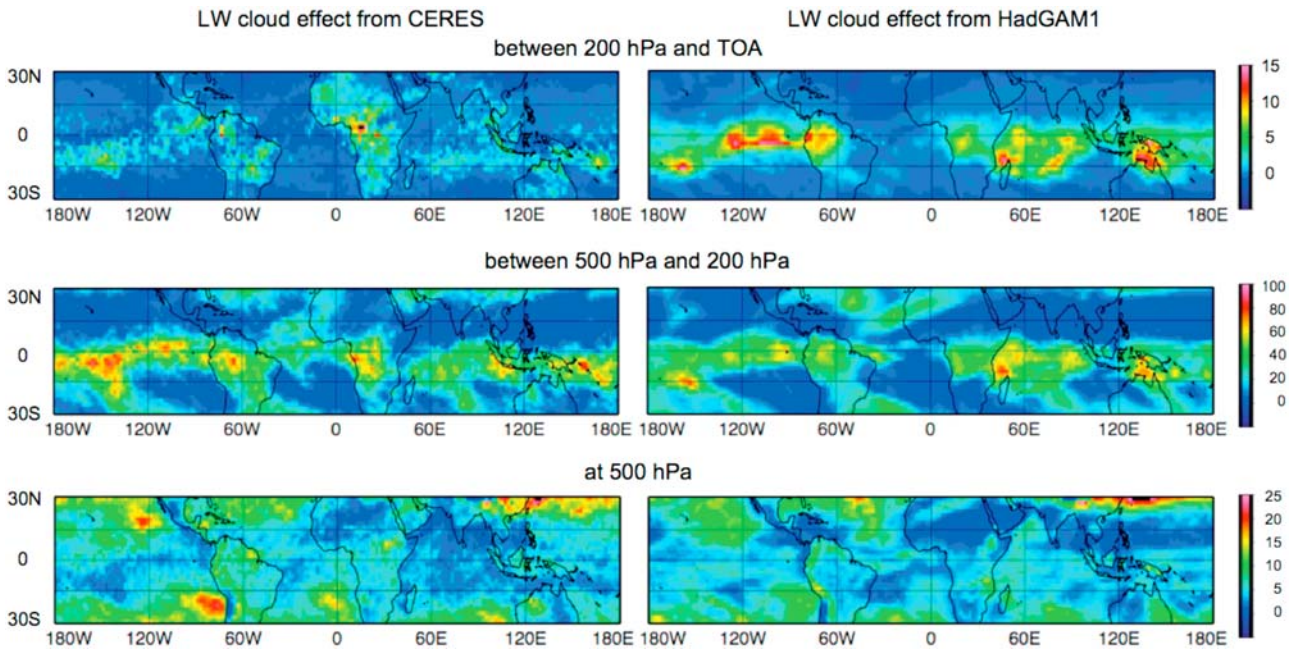

Figure 10. LW cloud effect between different levels for March 1998. (left) CERES SARB and (right) HadGAM1. (top) Cloud effects between 200 hPa and TOA; (middle) cloud effects between 500 hPa and 200 hPa; (bottom) cloud effects at 500 hPa. Units are watts per meters squared.

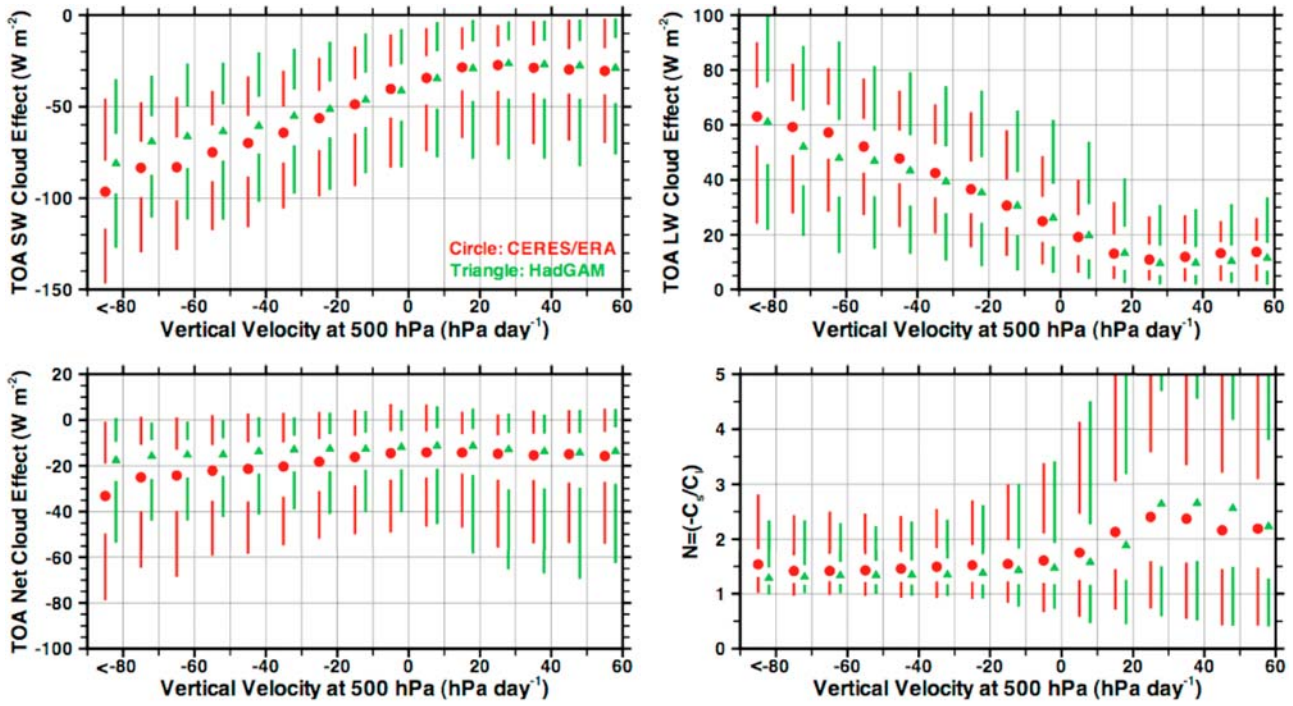

Figure 11. TOA SW cloud effect (C_S), LW cloud effect (C_L), net cloud effect (C_N), and the ratio $N = -C_S/C_L$ stratified by vertical velocity at 500 hPa. We used all 8 months CERES SARB data on the TRMM satellite. SARB cloud effects and N are stratified by vertical velocity from European Centre for Medium-Range Weather Forecasts ERA Interim reanalysis data (red lines with circle medians). HadGAM1 cloud effects and N are stratified by their own vertical velocity (green lines with triangle medians). Symbols are the median values for each circulation regime, the top and bottom of the upper vertical lines are the 95th percentiles and upper quartiles, and the top and bottom of the lower vertical lines are the lower quartiles and the 5th percentiles.

reflective hot surfaces. HadGAM1 simulates the frequency (within 1%) and locations of this net warming effect exceptionally well.

4. Conclusions

[41] In this study, the vertical radiative flux profiles and the cloud radiative effects at different levels from HadGAM1 over the tropics (30°S–30°N) have been compared to those derived from CERES SARB data on TRMM satellite from January to August 1998. Comparisons of the flux and cloud effect profiles, in addition to those at the TOA, enable us to evaluate the averaged cloud height and cloudiness within a layer in HadGAM1. Attributing the differences in cloud effects to the cloud height and cloudiness within multiple layers provides information to better pinpoint the deficiencies in convective parameterization (pertinent to convective detrainment levels), and the deficiencies in low cloud parameterization (from the cloud height and cloudiness comparisons), which will eventually lead to improvements in the related aspects of parameterizations in the model.

[42] The monthly tropical mean all-sky downwelling SW flux ($S_a^{\downarrow}$) from HadGAM1 agrees with that from CERES SARB to within 1.5 W m^{-2} at 70 hPa and 200 hPa, but HadGAM1 has larger overestimation of $S_a^{\downarrow}$ at the surface and 500 hPa, with the maximum difference of 12.7 W m^{-2} occurs at 500 hPa. Since SARB tends to overestimate the SW surface insolation, the actually overestimation of $S_a^{\downarrow}$ by HadGAM1 at the surface could be on the order of 10 to 20 W m^{-2}. The monthly tropical mean all-sky upwelling LW flux ($L_a^{\uparrow}$) from HadGAM1 agrees with that from CERES SARB to within 2.0 W m^{-2} at 500 hPa, but HadGAM1 has larger overestimation of $L_a^{\uparrow}$ at the other four levels, with the maximum difference of 9.0 W m^{-2} occuring at TOA, which is much larger than the inherent uncertainty of SARB data. Large regional differences between HadGAM1 and CERES SARB occur over major convective and stratocumulus regions.

[43] One novelty of this investigation is an analysis of cloud radiative effects within the atmosphere, as well as the TOA. At TOA HadGAM1 underestimates the monthly tropical mean SW cloud effects by 1 to 4 W m^{-2} comparing to those derived from CERES SARB, indicating a general lack of cloudiness in the model. Does the model lack low, middle, or high clouds? Radiative flux profiles make it possible to decompose TOA cloud effects into different layers: at 500 hPa, between 500 and 200 hPa, and between 200 hPa and TOA. Comparisons of monthly tropical mean cloud effects within these layers suggest that the lack of clouds in HadGAM1 happens mainly between 500 and 200 hPa. The monthly tropical mean SW cloud effects at 500 hPa from CERES SARB and HadGAM1 agree to within 1 W m^{-2}, indicating either the cloud fraction and optical depth at heights below 500 hPa from HadGAM1 are in good agreement with those retrievals used in CERES SARB, or there are compensating effects between cloud fraction and optical depth in HadGAM1, or compensating regional effects in the model. The monthly tropical mean SW cloud effects between 200 hPa and TOA from HadGAM1 are larger than those from CERES, indicating the model produces more clouds above 200 hPa.

[44] Also, if N, the ratio of SW to LW cloud effects, is assessed only at the TOA, the HadGAM1 simulates the column averaged cloud heights in the tropics exceptionally well (within 8% of those from CERES SARB). Comparing to its predecessor, HadAM3, HadGAM1 has a better skill in simulating cloud effects, because of its smaller differences in LW and net cloud effects and N values from obervations. However, N values at the three layers within the atmosphere indicate that HadGAM1 consistently underestimates averaged cloud height for clouds at height below 500 hPa and consistently overestimates that for clouds between 500 and 200 hPa. The comparison is not conclusive for clouds above 200 hPa.

[45] We further stratify the cloud effects by vertical velocity at 500 hPa to understand the cloud effect differences in relation to dynamic regimes. We find that the lack of cloudiness in HadGAM1 mainly occurs in the convective regimes, and it has more clouds than CERES SARB in the subsidence regimes. In addition, the stratified N suggests that column averaged cloud heights from HadGAM1 are higher than those from SARB in the convective regimes, but the reverse is true for the strong subsidence regimes.

[46] Although this study used CERES TRMM data product, the newly released monthly regional radiative fluxes and clouds (AVG) data set for CERES on Terra and Aqua can also be used to evaluate the flux profiles and cloud effect profiles from GCMs. With the availability of cloud profiling data from active sensors, such as Cloud-Aerosol Lidar and Infrared Pathfinder Satellite Observations (CALIPSO) and CloudSat, direct evaluation of GCM cloud vertical structures becomes possible. Additionally, vertical structures from CALIPSO and CloudSat can be included in the vertical flux profile calculations, which can be compared with the flux profiles from the standard CERES SARB product. We can assess the accuracies of the flux profiles in the CERES SARB product from these comparisons, which will increase our confidence in evaluating the vertical profiles of radiative flux and cloud radiative effects from GCMs. The present study has provided the first attempt and should be extended to more recent periods when cloud profiling data from active sensors become available.

[47] **Acknowledgments.** This research was funded by the Clouds and the Earth's Radiant Energy System (CERES) project. The authors thank Mark Ringer, Fred Rose, David Rutan, David Kratz, and Zachary Eitzen for helpful discussions. A.B. was supported by the Defra and MoD Integrated Climate Program (Defra, GA01101; MoD, CBC/2B/0417_Annex C5). K.-M.X. acknowledges the support of the NASA Modeling, Analysis, and Prediction Program. The CERES data were obtained from the Atmospheric Sciences Data Center at the NASA Langley Research Center. ECMWF ERA-Interim data used in this study have been obtained from the ECMWF data server.

References

Allan, R. P., and M. A. Ringer (2003), Inconsistencies between satellite estimates of longwave cloud forcing and dynamical fields from reanalyses, *Geophys. Res. Lett.*, *30*(9), 1491, doi:10.1029/2003GL017019.

Allan, R. P., A. Slingo, and M. A. Ringer (2002), Influence of dynamics on the changes in tropical cloud radiative forcing during the 1998 El Niño, *J. Clim.*, *15*, 1979–1986.

Barker, H. W., and Z. Li (1995), Improved simulation of clear-sky shortwave radiative transfer in the CCC-GCM, *J. Clim.*, *8*, 2213–2223.

Barkstrom, B. R., E. F. Harrison, G. Smith, R. Green, J. Kibler, R. D. Cess, and the ERBE Science Team (1989), Earth Radiation Budget Experiment (ERBE) archival and April 1985 results, *Bull. Am. Meteorol. Soc.*, *70*, 1254–1262.

Bodas-Salcedo, A., M. A. Ringer, and A. Jones (2008), Evaluation of the surface radiation budget in the atmospheric component of the Hadley Center Global Environmental Model (HadGEM1), *J. Clim.*, *21*, 4723–4748, doi:10.1175/2008JCLI2097.1.

Bony, S., and J.-L. Dufresne (2005), Marine boundary layer clouds at the heart of tropical cloud feedback uncertainties in climate models, *Geophys. Res. Lett.*, *32*, L20806, doi:10.1029/2005GL023851.

Bony, S., H. Le Treut, J.-P. Duvel, and R. S. Kandel (1992), Satellite validation of GCM-simulated annual cycle of the Earth radiation budget and cloud forcing, *J. Geophys. Res.*, *97*, 18,061–18,081.

Bony, S., J.-L. Dufresne, and H. Le Treut (2004), On dynamic and thermodynamic components of the cloud changes, *Clim. Dyn.*, *22*, 71–86.

Cess, R. D., M. Zhang, P.-H. Wang, and B. A. Wielicki (2001a), Cloud structure anomalies over the tropical Pacific during the 1997/98 El Niño, *Geophys. Res. Lett.*, *28*, 4547–4550.

Cess, R. D., M. Zhang, B. A. Wielicki, D. F. Young, X. L. Zhou, and Y. Nikitenko (2001b), The influence of the 1998 El Niño upon cloud-radiative forcing over the Pacific warm pool, *J. Clim.*, *14*, 2129–2137.

Charlock, T. P., F. G. Rose, D. A. Rutan, Z. Jin, and S. Kato (2006), The global surface and atmosphere radiation budget: An assessment of accuracy with 5 years of calculations and observations, paper presented at the 12th Conference on Atmospheric Radiation, Am. Meteorol. Soc., Madison, Wis.

Clough, S. A., M. J. Iacono, and J. L. Moncet (1992), Line-by-line calculations of atmospheric fluxes and cooling rates: Application to water vapor, *J. Geophys. Res.*, *97*, 15,761–15,785.

Collins, W. D., P. J. Rasch, B. E. Eaton, B. V. Khattatov, J.-F. Lamarque, and C. S. Zender (2001), Simulating aerosols using a chemical transport model with assimilation of satellite aerosol retrievals: Methodology for INDOEX, *J. Geophys. Res.*, *106*, 7313–7336.

Davies, T., M. J. P. Cullen, A. J. Malcolm, M. H. Mawson, A. Stainforth, A. A. White, and N. Wood (2005), A new dynamical core for the Met Office's global and regional modeling of the atmosphere, *Q. J. R. Meteorol. Soc.*, *131*, 1759–1782, doi:10.1256/qj.04.101.

Edwards, J. M., and A. Slingo (1996), Studies with a flexible new radiation code. I: Choosing a configuration for a large-scale model, *Q. J. R. Meteorol. Soc.*, *122*, 689–720.

Edwards, J. M., S. Havemann, J. C. Thelen, and A. J. Baran (2007), A new parametrization for the radiative properties of ice crystals: Comparison with existing schemes and impact in a GCM, *Atmos. Res.*, *83*, 19–35, doi:10.1016/j.atmosres.2006.03.02.

Essery, R. L. H., M. J. Best, R. A. Betts, P. M. Cox, and C. M. Taylor (2003), Explicit representation of subgrid heterogeneity in a GCM land-surface scheme, *J. Hydrometeorol.*, *4*, 530–543.

Fu, Q., and K.-N. Liou (1992), On the correlated-k distribution method for radiative transfer in nonhomogenous atmospheres, *J. Atmos. Sci.*, *49*, 2139–2156.

Fu, Q., and K.-N. Liou (1993), Parameterization of the radiative properties of cirrus clouds, *J. Atmos. Sci.*, *50*, 2008–2025.

Gates, W. L., et al. (1999), An overview of the results of the Atmospheric Model Intercomparison Project (AMIP I), *Bull. Am. Meteorol. Soc.*, *80*, 29–55.

Harrison, E. F., P. Minnis, B. R. Barkstrom, V. Ramanathan, R. D. Cess, and G. G. Gibson (1990), Seasonal variation of cloud radiative forcing derived from the Earth Radiation Budget Experiment, *J. Geophys. Res.*, *95*, 18,687–18,703.

Holz, R. E., S. A. Ackerman, F. W. Nagle, R. Frey, S. Dutcher, R. E. Kuehn, M. A. Vaughan, and B. Baum (2008), Global Moderate Resolution Imaging Spectroradiometer (MODIS) cloud detection and height evaluation using CALIOP, *J. Geophys. Res.*, *113*, D00A19, doi:10.1029/2008JD009837.

Ignatov, A., and L. Stowe (2000), Physical basis, premises, and self-consistency checks of aerosol retrievals from TRMM VIRS, *J. Appl. Meteorol.*, *39*, 2259–2277.

Kiehl, J. T., and V. Ramanathan (1990), Comparison of cloud forcing derived from the Earth Radiation Budget Experiment with that simulated by the NCAR GCM, *J. Geophys. Res.*, *95*, 11,679–11,698.

Kristjánsson, J. E., J. M. Edwards, and D. L. Mitchell (2000), Impact of a new scheme for optical properties of ice crystals on climates of two GCMs, *J. Geophys. Res.*, *105*, 10,063–10,079.

Lin, X., L. D. Fowler, and D. A. Randall (2002), Flying the TRMM satellite in a general circulation model, *J. Geophys. Res.*, *107*(D16), 4281, doi:10.1029/2001JD000619.

Loeb, N. G., N. Manalo-Smith, S. Kato, W. F. Miller, S. K. Gupta, P. Minnis, and B. A. Wielicki (2003a), Angular distribution models for top-of-atmosphere radiative flux estimation from the Clouds and the Earth's Radiant Energy System instrument on the Tropical Rainfall Measuring Mission satellite. Part I: Methodology, *J. Appl. Meteorol.*, *42*, 240–265.

Loeb, N. G., K. Loukachine, N. Manalo-Smith, B. A. Wielicki, and D. F. Young (2003b), Angular distribution models for top-of-atmosphere radiative flux estimation from the Clouds and the Earth's Radiant Energy System instrument on the Tropical Rainfall Measuring Mission satellite. Part II: Validation, *J. Appl. Meteorol.*, *42*, 1748–1769.

Lu, R., B. Dong, R. D. Cess, and G. L. Potter (2004), The 1997/98 El Niño: A test for climate models, *Geophys. Res. Lett.*, *31*, L12216, doi:10.1029/2004GL019956.

Mace, G. G., Y. Zhang, S. Platnick, M. D. King, P. Minnis, and P. Yang (2005), Evaluation of cirrus cloud properties derived from MODIS data using cloud properties derived from ground-based observations collected at the ARM SGP site, *J. Appl. Meteorol.*, *44*, 221–240.

Martin, G. M., M. A. Ringer, V. D. Pope, A. Jones, C. Dearden, and T. J. Hinton (2006), The physical properties of the atmosphere in the new Hadley center global environmental model (HadGEM1). Part I: Model description and global climatology, *J. Clim.*, *19*, 1274–1301.

Minnis, P., W. L. J. Smith, D. P. Garber, J. K. Ayers, and D. R. Doelling (1995), Cloud properties derived from GOES-7 for the spring 1994 ARM intensive observing period using version 1.0.0 of the ARM satellite data analysis program, *NASA Tech. Rep., NASA RP-1366*.

Minnis, P., D. P. Garber, D. F. Young, R. F. Arduini, and Y. Takano (1998), Parameterizations of reflectance and effective emittance for satellite remote sensing of cloud properties, *J. Atmos. Sci.*, *55*, 3313–3339.

Minnis, P., J. Huang, B. Lin, Y. Yi, R. F. Arduini, T.-F. Fan, J. K. Ayers, and G. G. Mace (2007), Ice cloud properties in ice-over-water cloud systems using Tropical Rainfall Measuring Mission (TRMM) visible and infrared scanner and TRMM Microwave Imager data, *J. Geophys. Res.*, *112*, D06206, doi:10.1029/2006JD007626.

Minnis, P., Q. Z. Trepte, S. Sun-Mack, Y. Chen, D. R. Doelling, D. F. Young, D. A. Spangenberg, W. F. Miller, B. A. Wielicki, R. R. Brown, S. C. Gibson, and E. B. Geier (2008), Cloud detection in nonpolar regions for CERES using TRMM VIRS and TERRA and AQUA MODIS data, *IEEE Trans. Geosci. Remote Sens.*, *46*, 3857–3884.

Mlawer, E. J., et al. (2004), Recent developments on the broadband heating rate profile value-added-product, paper presented at the 13th ARM Science Team Meeting, Broomfield, Colo.

Norris, J. R., and C. P. Weaver (2001), Improved techniques for evaluation GCM cloudiness applied to the NCAR CCM3, *J. Clim.*, *14*, 2540–2550.

Pinker, R. T., and I. Laszlo (1992), Modeling surface solar irradiance for satellite applications on global scale, *J. Appl. Meteorol.*, *31*, 194–211.

Pope, V. D., M. L. Gallani, P. R. Rowntree, and R. A. Stratton (2000), The impact of new physical parameterizations in the Hadley Center climate model: HadAM3, *Clim. Dyn.*, *16*, 123–146.

Rabier, F., J.-N. Thepaut, and P. Courtier (1998), Extended assimilation and forecast experiments with a four-dimensional variational assimilation, *Q. J. R. Meteorol. Soc.*, *124*, 1861–1887.

Ringer, M. A., and R. P. Allan (2004), Evaluating climate model simulations of tropical cloud, *Tellus, Ser. A*, *56*, 308–327.

Ringer, M. A., et al. (2006), The physical properties of the atmosphere in the new Hadley Centre Global Environmental Model (HadGEM1). Part II: Aspects of variability and regional climate, *J. Clim.*, *19*, 1302–1326.

Rose, F. G., and T. P. Charlock (2002), New Fu-Liou code tested with ARM Raman Lidar and CERES in pre-CALIPSO exercise, paper presented at the 11th Conference on Atmospheric Radiation, Am. Meteorol. Soc., Ogden, Utah.

Rossow, W. B., and R. A. Schiffer (1991), ISCCP cloud data products, *Bull. Am. Meteorol. Soc.*, *72*, 2–20.

Rothman, L. S. (2003), The HITRAN molecular spectroscopic database: Edition of 2000 including updates through 2001, *J. Quant. Spectrosc. Radiat. Transfer*, *82*, 5–44, doi:10.1016/S0022-4073(03)00146-8.

Rutan, D., and T. P. Charlock (2004), Validation of CERES/SARB data product using ARM surface flux observations, paper presented at the 14th ARM Science Team Meeting, Albuquerque, N. M.

Rutan, D., F. Rose, T. P. Charlock, E. Mlawer, T. Shippert, and S. Kato (2006), Broadband heating rate product flux profiles compared to Clouds and the Earth's Radiant Energy System radiation transfer data product, paper presented at the 14th ARM Science Team Meeting, Albuquerque, N. M.

Su, W., T. P. Charlock, and F. G. Rose (2005), Derving surface ultraviolet radiation from CERES surface and atmospheric radiation budget: Methodology, *J. Geophys. Res.*, *110*, D14209, doi:10.1029/2005JD005794.

Su, W., T. P. Charlock, F. G. Rose, and D. Rutan (2007), Photosynthetically active radiation from clouds and the Earth's radiant energy system (CERES) products, *J. Geophys. Res.*, *112*, G02022, doi:10.1029/2006JG000290.

Suttles, J. T., et al. (1988), Angular radiation models for Earth-atmosphere system, vol. 1, Shortwave radiation, *NASA Tech. Rep., NASA RP-1184*.

Suttles, J. T., et al. (1989), Angular radiation models for Earth-atmosphere system, vol. 3, Longwave radiation, *NASA Tech. Rep., NASA RP-1184*.

Tselioudis, G., Y. Zhang, and W. B. Rossow (2000), Cloud and radiation variations associated with northern midlatitude low and high sea level pressure regimes, *J. Clim.*, *13*, 312–327.

Uppala, S., D. Dee, S. Kobayashi, P. Berrisford, and A. Simmons (2008), Toward a climate data assimilation system: Status update of ERA-Interim, *ECMWF Newsl.*, *115*, 12–18.

Webb, M., C. Senior, S. Bony, and J.-J. Morerette (2001), Combining ERBE and ISCCP data to assess clouds in the Hadley Centre, ECMWF and LMD atmospheric climate models, *Clim. Dyn.*, *17*, 905–922.

Whitlock, C. H., et al. (1995), First global WCRP shortwave surface radiation budget data set, *Bull. Am. Meteorol. Soc.*, *76*, 905–922.

Wielicki, B. A., B. R. Barkstrom, E. F. Harrison, R. B. Lee, G. L. Smith, and J. E. Cooper (1996), Clouds and the Earth's Radiant Energy System (CERES): An Earth Observing System experiment, *Bull. Am. Meteorol. Soc.*, *77*, 853–868.

Wild, M., A. Ohmura, H. Gilgen, and E. Roeckner (1995), Validation of GCM simulated radiative fluxes using surface observations, *J. Clim.*, *8*, 1309–1324.

Wild, M., C. N. Long, and A. Ohmura (2006), Evaluation of clear-sky solar fluxes in GCMs participating in AMIP and IPCC-AR4 from a surface perspective, *J. Geophys. Res.*, *111*, D01104, doi:10.1029/2005JD006118.

Williams, K. D., and G. Tselioudis (2007), GCM intercomparison of global cloud regimes: Present-day evaluation and climate change response, *Clim. Dyn.*, *29*, 231–250, doi:10.1007/s00382-007-0232-2.

Williams, K. D., M. A. Ringer, and C. A. Senior (2003), Evaluating the cloud response to climate change and current climate variability, *Clim. Dyn.*, *20*, 705–721, doi:10.1007/s00382-002-0303-3.

Williams, K. D., C. A. Senior, A. Slingo, and J. F. B. Mitchell (2005), Toward evaluating cloud response to climate change using clustering technique identifications of cloud regimes, *Clim. Dyn.*, *24*, 701–719, doi:10.1007/s00382-004-0512-z.

Wong, T., D. F. Young, M. Haeffelin, and S. Weckmann (2000), Validation of the CERES/TRMM ERBE-Like monthly mean clear-sky longwave dataset and the effects of the 1998 ENSO event, *J. Clim.*, *13*, 4256–4267.

Yuan, J., D. L. Hartmann, and R. Wood (2008), Dynamic effects on the tropical cloud radiative forcing and radiation budget, *J. Clim.*, *21*, 2337–2351, doi:10.1175/2007JCLI1857.1.

Zhang, Y., W. B. Rossow, and A. A. Lacis (1995), Calculation of surface and top of atmosphere radiative fluxes from physical quantities based on ISCCP datasets I. Method and sensitivity to input data uncertainties, *J. Geophys. Res.*, *100*, 1149–1165.

Zhang, Y., W. B. Rossow, A. A. Lacis, V. Oinas, and M. I. Mishchenko (2004), Calculation of radiative fluxes from the surface and top of atmosphere based on ISCCP and other global data sets: Refinements of the radiative transfer model and input data, *J. Geophys. Res.*, *109*, D19105, doi:10.1029/2003JD004457.

A. Bodas-Salcedo, Met Office, Hadley Center, FitzRoy Road, Exeter EX1 3PB, UK.

T. P. Charlock, W. Su, and K.-M. Xu, MS420, NASA Langley Research Center, Hampton, VA 23681, USA. (wenying.su-1@nasa.gov)